Tunable unconventional spin orbit torque magnetization dynamics in van der Waals heterostructures

(article starts on next page)

Tunable unconventional spin orbit torque magnetization dynamics in van der Waals heterostructures

Lalit Pandey [1,2] ✉, Bing Zhao [1], Karma Tenzin [3,4], Roselle Ngaloy[1], Veronika Lamparská[3], Himanshu Bangar[1], Aya Ali[5], Mahmoud Abdel-Hafiez [6,7,8], Gaojie Zhang[9], Hao Wu[9], Haixin Chang [9], Lars Sjöström [1], Prasanna Rout [1], Jagoda Sławińska [3] & Saroj P. Dash [1,2,10] ✉

Two-dimensional quantum material heterostructures can offer a promising platform for energy-efficient non-volatile spin-based technologies. However, spin dynamics experiments to understand the basic spin-orbit torque phenomena are so far lacking. Here, we demonstrate unconventional out-of-plane magnetization dynamics, and energy-efficient and field-free spin-orbit torque switching in a van der Waals heterostructure comprising out-of-plane magnet Fe_3GaTe_2 and topological Weyl semimetal $TaIrTe_4$. We measured non-linear second harmonic Hall signal in $TaIrTe_4/Fe_3GaTe_2$ devices to evaluate the magnetization dynamics, which is characterized by large and tunable out-of-plane damping-like torque. Energy-efficient and deterministic field-free SOT magnetization switching is achieved at room temperature with a very low current density. First-principles calculations unveil the origin of the unconventional charge-spin conversion phenomena, considering the crystal symmetry and electronic structure of $TaIrTe_4$. These results establish that van der Waals heterostructures provide a promising route to energy-efficient, field-free, and tunable spintronic devices.

In quantum materials, the interplay between spin-orbit coupling and magnetism, with additional control over the band topology, quantum geometries, and crystal symmetries can offer the potential for next-generation universal memory and computing technologies[1,2]. Specifically, enhanced functionalities can be achieved using efficient charge-spin conversion (CSC) phenomena in such quantum materials to enable spin-orbit torque (SOT) induced magnetization switching of a ferromagnet (FM)[3]. In conventional SOT memory devices, commonly used spin-orbit materials (SOM) exhibit moderate CSC efficiency and primarily generate in-plane SOT torque components, limiting their application in switching a magnet with perpendicular magnetic anisotropy (PMA)[4].

Recently developed van der Waals (vdW) heterostructures of two-dimensional (2D) SOMs and FMs can offer an alternative framework to address the challenges in SOT technologies[5]. Interestingly, low crystal symmetries of vdW SOMs can generate out-of-plane SOT components,

making them suitable for field-free switching of ferromagnets with PMA[6–9]. Meanwhile, vdW magnets such as Fe_3GeTe_2 and Fe_3GaTe_2 with strong PMA are also developed, showing promise for reliable SOT device operations[10–13]. Taking advantage of such quantum materials, all-2D vdW heterostructures have been explored for field-free SOT magnetization switching[14–17]. However, the SOT switching parameters are two to three orders of magnitude lower than required for energy-efficient switching and most of the experiments were limited to cryogenic temperatures.

To circumvent this issue, Weyl semimetal $TaIrTe_4$ with low crystal symmetry, large spin-orbit coupling (SOC), and large Berry curvature dipole was explored to generate a larger out-of-plane SOT component for energy-efficient and field-free SOT switching of conventional magnets[8,9,18]. Therefore, all-2D vdW heterostructure combining the best vdW quantum materials with a large current-induced out-of-plane spin polarization and above room temperature vdW ferromagnet with an out-of-plane magnetization is encouraging for energy-efficient non-volatile spintronic technologies. Furthermore, the investigation of magnetization dynamics in all-2D vdW heterostructures is critical for understanding the interplay between broken crystal symmetries, unconventional CSC, and SOT-induced magnetization dynamics, ultimately enabling the design of efficient and ultrafast spintronic devices.

Here, we show strong unconventional out-of-plane SOT magnetization dynamics using harmonic measurements and demonstrate energy-efficient field-free SOT magnetization switching using the all-vdW heterostructures of $TaIrTe_4/Fe_3GaTe_2$ at room temperature. Weyl semimetal $TaIrTe_4$ with a tunable canted spin polarization combined with a vdW ferromagnet Fe_3GaTe_2 with strong PMA enables the exploration of magnetization dynamics and their tunable SOT efficiency. The 2nd harmonic measurements with detailed magnetic field and angle-dependent measurements at various temperatures reveal a large and tunable unconventional out-of-plane SOT torque in the $TaIrTe_4/Fe_3GaTe_2$ all-vdW heterostructure. The SOT components are observed to vary with temperature and correlate with the measured spin canting angle. Moreover, we observed a field-free deterministic SOT magnetization switching with a very low critical switching current density of $1.81 \times 10^{10} A/m^2$, demonstrating energy-efficient non-volatile spintronic memory device. To unveil the origin of the unconventional CSC phenomena in $TaIrTe_4$, detailed first-principles calculations were performed considering crystal symmetry and electronic structures.

Results

We investigated $TaIrTe_4/Fe_3GaTe_2$ vdW heterostructures (Fig. 1a)[19] due to their promising properties, anticipating that their combination could yield contemporary phenomena such as large non-linear Hall effects and unconventional spin-orbit torque (SOT) magnetization dynamics. $TaIrTe_4$ is a vdW topological Weyl semimetal (WSM) candidate, with a significant Berry curvature dipole and large spin splitting of the electronic bands[20]. In addition, it provides unconventional charge-spin conversion with an out-of-plane spin polarization component that can induce an out-of-plane SOT[18] on the adjacent PMA ferromagnet to induce a magnetic field-free switching. On the other hand, Fe_3GaTe_2 is a unique vdW topological nodal line metallic ferromagnet with strong
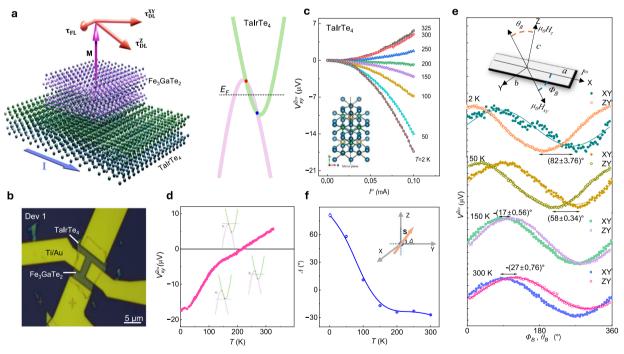

Fig. 1 | Van der Waals heterostructure of $TaIrTe_4/Fe_3GaTe_2$ and harmonic measurements on $TaIrTe_4$. a Schematic diagram of a van der Waals (vdW) heterostructure of Weyl semimetal $TaIrTe_4$ and out-of-plane ferromagnet Fe_3GaTe_2. Band structure of typical type-II Weyl semimetal with two Weyl nodes. **b** Optical image of representative $TaIrTe_4/Fe_3GaTe_2$ vdW heterostructure Hall bar device with a scale bar of 5 μm. **c** 2nd harmonic transverse Hall voltage $V_{xy}^{2\omega}$ in response to an applied alternating current I^ω along a-axis at different temperatures for a device with 20 nm thin $TaIrTe_4$. The inset illustrates the crystal structure of T_d-$TaIrTe_4$, characterized by low crystal symmetry and a mirror plane along the crystallographic b-axis. **d** 2nd harmonic transverse Hall voltage $V_{xy}^{2\omega}$ with temperature at an I^ω of 0.1 mA of $TaIrTe_4$. Insets show the energy dispersion curve of type-II Weyl semimetal and tuning of Fermi level energy (E_F) with temperature. **e** 2nd harmonic

voltage $V^{2\omega}$ response measured in $TaIrTe_4$ device as a function of angle between current applied along a-axis of $TaIrTe_4$ ($|I^\omega| = 0.1$ mA) and external magnetic field (13 T). The device is rotated in XY and ZY planes, as depicted in the schematics. In the XY rotation, the device rotates such that the magnetic field aligns parallel to the sample surface and making Φ_B angle with a-axis of $TaIrTe_4$, whereas in ZY rotation, the device rotation changes magnetic field direction from a-axis of $TaIrTe_4$ to c axis and making θ_B angle with c-axis with $TaIrTe_4$. The solid lines are the fits.
f Temperature dependence of shift (Δ) in the maxima or minima of $V^{2\omega}$ vs Φ_B and θ_B curves. This shift is denoted as out-of-plane canting angles, as illustrated in schematics. Such shift is directly correlated to the out-of-plane spin canting angle, which is estimated to be $-(27 \pm 0.76)°$ at room temperature. Error bars in **f** are obtained by fitting experimental data in **e** using $\sin\Phi_B$ and $\sin(\theta_B + \Delta)$ functions.
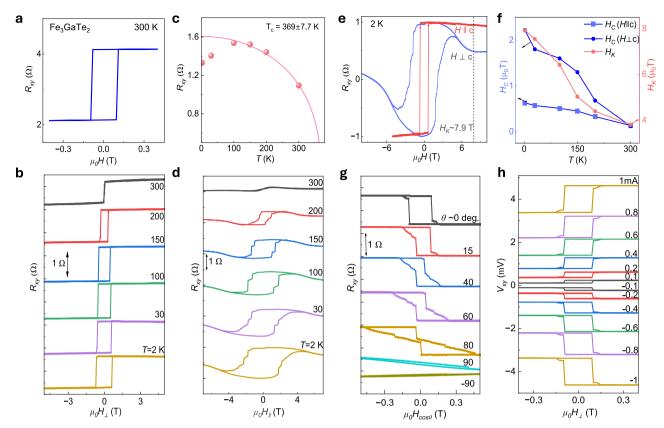
Fig. 2 | Magneto-transport characterization of Fe₃GaTe₂. a, b Anomalous Hall resistance of Fe_3GaTe_2 as a function of out-of-plane magnetic fields at 300 K and temperature dependence ranging from 2 to 300 K. **c** Anomalous Hall amplitude at the saturated field as a function of temperature. Solid line is fit to extract the Curie temperature ($T_c = 369.14 \pm 7.73K$) **d** Anomalous Hall resistance of Fe_3GaTe_2 as a function of in-plane magnetic fields at different temperatures ranging from 2 to 300 K. **e** Comparison of anomalous Hall effect measurement for field swept parallel to sample plane (i.e., $H\perp c$) vs perpendicular (i.e., $H\|c$) to sample plane at 2 K temperature. The anisotropic field (H_K) is -7.9 T, indicating strong perpendicular magnetic anisotropy present in Fe_3GaTe_2. **f** Variation of coercive fields and anisotropic fields with temperature extracted from (R_{xy} vs $\mu_0 H_\perp$) and (R_{xy} vs $\mu_0 H_\|$) measurements. **g** AHE signals R_{xy} with different out-of-plane angles (θ) between the magnetic field and the c-axis of the sample plane at 300 K. **h** Variation of AHE signals R_{xy} with positive and negative DC bias currents.

PMA above room temperature with T_c around 370 K[10]. We fabricated Hall-bar devices based on $TaIrTe_4$/Fe_3GaTe_2 vdW heterostructures, along with individual Hall bars on $TaIrTe_4$ and Fe_3GaTe_2 crystals, to characterize properties, such as the anomalous Hall effect (AHE), 2nd harmonics measurements and SOT-driven switching experiments (details in Methods section and Supplementary Fig. S1). Figure 1b presents a typical optical microscope image of a representative $TaIrTe_4$/Fe_3GaTe_2 Hall-bar device.

Tunable spin texture using bilinear magnetoresistance and 2nd harmonic Hall effect in TaIrTe₄

$TaIrTe_4$ exhibited a strong nonlinear Hall effect, characterized by a 2nd harmonic Hall voltage that nonlinearly depends on driving currents sourced along the a-axis of the crystal, perpendicular to its mirror plane at room temperature (Fig. 1c). Unlike linear Hall effects observed in systems with broken time-reversal symmetry, the nonlinear Hall effect in $TaIrTe_4$ arises from the large Berry curvature dipole in the absence of inversion-symmetry (also see Supplementary Note 2). Notably, the nonlinear Hall voltage changed sign near ~200 (Fig. 1c, d), indicating temperature-induced shift in the chemical potential, consistent with the Weyl semi-metallic properties of $TaIrTe_4$[21]. The current induced spin polarization in $TaIrTe_4$ are probed using bilinear magnetoelectric resistance (BMER) technique[9,22], measuring 2nd harmonic voltage while rotating the samples in XY and ZY planes (Fig. 1e). In XY rotation, the magnetic field vector remains in the ab crystallographic plane sweeping azimuthal angle (Φ_B) with respect to the a-axis of $TaIrTe_4$, whereas in ZY rotation, the field vector sweeps polar angle (θ_B) with respect to the c-axis of $TaIrTe_4$ in the ac plane. Figure 1e depicts the temperature dependence of 2nd harmonic voltage with Φ_B and θ_B. The direction of resultant spin angular momentum arises due to CSC effects in $TaIrTe_4$ being equivalent to angular shift (Δ) of BMER curves measured along XY and ZY geometries. The Δ is found to be $-(27 \pm 0.76)°$ at room temperature, indicating the presence of an out-of-plane spin density induced in $TaIrTe_4$. Such spin-polarization can help in generating unconventional out-of-plane SOT in adjacent ferromagnetic layer Fe_3GaTe_2 with PMA resulting in field-free deterministic switching. The temperature dependence of Δ (Fig. 1f) suggests that the polarity and magnitude of the spin canting angle in $TaIrTe_4$ are highly tunable by the position of chemical potential/Fermi level[9].

Perpendicular magnetic anisotropy of Fe₃GaTe₂

To verify the magnetic property and anisotropy of Fe_3GaTe_2, the anomalous Hall resistance R_{xy} is measured at different temperatures ranging from 2 to 300 K (Fig. 2a, b). A square-shaped magnetic hysteresis loop is observed with coercivity around 100 mT and anomalous Hall resistance (R_{AHE}) of around 1.5 Ω at room temperature, where the latter is directly proportional to saturation magnetization (M_s) of Fe_3GaTe_2. The R_{AHE} vs T curve, shown in Fig. 2c, is fitted with

$$R_{xy}(T) = R_{xy}(0)\left(1 - \left(\frac{T}{T_c}\right)^2\right)^{\beta}$$ analogues to Bloch equation for magnetization vs temperature curve to estimate Curie temperature ($T_c = 369.14 \pm 7.73K$)[10] and critical magnetization exponent $\beta = 0.35$[22-26]. Figure 2d shows the anomalous Hall resistance of

Fe$_3$GaTe$_2$ as a function of in-plane magnetic fields at different temperatures from 2 to 300 K. A magnetic hysteresis loop is observed at all temperatures, with finite remanence and coercivity, consistent with the typical behavior of PMA magnets along their hard axis (Fig. 2e).

Figure 2f shows the variation of magnetic coercivity (H_c) in both field directions (i.e., $H \perp c - axis$ and $H || c - axis$) and anisotropic field with temperature. The anisotropic field (H_K), defined as the difference in saturation between in-plane and out-of-plane magnetic fields, reaches ~7.9 T at 2 K and ~3.8 T at 300 K. Such a high value of H_K suggests that Fe$_3$GaTe$_2$ has a very high magnetic anisotropy energy density with a very strong PMA. The coercive field (H_c) is also quite high along in-plane direction as compared to out-of-plane direction. Both the H_c and H_K decrease with an increase in temperature approaching the Curie temperature of Fe$_3$GaTe$_2$. Figure 2g illustrates AHE signals R_{xy} measured at varying out-of-plane angles (θ) between c-axis of sample and magnetic field. It can be noted here that the magnitude of AHE signal ($R_{xy}^{AHE} = \frac{R_{xy}(+H_S) - R_{xy}(-H_S)}{2}$) remains almost constant till ±80°; beyond that AHE loop disappears between ±600 mT field range. Again, this indicates a strong out-of-plane magnetic anisotropy present in Fe$_3$GaTe$_2$. Figure 2h shows the variation of AHE signals R_{xy} with positive and negative DC bias currents. We observed that the magnitude of anomalous Hall signal, the coercivity and saturation fields remain unchanged with positive or negative current bias varied from ±0.1 mA to ±1 mA, indicating the robustness of perpendicular anisotropic magnetic moment against dc current within these bias ranges.

2nd harmonic nonlinear Hall effect and spin-orbit torque induced magnetization dynamics in TaIrTe$_4$/Fe$_3$GaTe$_2$ heterostructures

The harmonic Hall measurements are performed on TaIrTe$_4$/Fe$_3$GaTe$_2$ heterostructures to quantitatively evaluate the non-linear effects and magnetization dynamics driven by SOT. When a sinusoidal current (I^ω) is applied to the vdW heterostructure, composed of the spin-orbit material TaIrTe$_4$ and a ferromagnet Fe$_3$GaTe$_2$, spin-orbit torques (τ_{SOT}) are exerted on the magnetization ($\mathbf{m}$) of the Fe$_3$GaTe$_2$. This effect originates from the spin accumulation at the vdW interface due to efficient CSC in TaIrTe$_4$. Typically, two mutually orthogonal torques are generated: the damping-like torque ($\tau_{DL} \sim \mathbf{m} \times (\sigma \times \mathbf{m})$) and the field-like torque ($\tau_{FL} \sim \sigma \times \mathbf{m}$)[13,27].

In these measurements, applying a sinusoidal current (I^ω) with a fixed frequency of 213.3 Hz induces SOT-driven magnetization oscillation, generating harmonics in both the longitudinal and transverse resistance signals. The 1st and 2nd harmonic signals are measured and analyzed across various angles (Φ_B) between the in-plane magnetic field ($H \perp c$) and the applied sinusoidal current (I^ω), as well as under varying external magnetic fields (H_{ext}). This analysis provides information about the current-induced effective SOT fields and torques.

Since the spin Hall effect (SHE) in TaIrTe$_4$ induces both in-plane and out-of-plane spin polarizations ($\sigma^{X,Y,Z}$), the applied I^ω along the a-axis of TaIrTe$_4$ generates corresponding components of the damping-like ($\tau_{DL}^{X,Y,Z}$) and field-like ($\tau_{FL}^{X,Y,Z}$) torques. The 2nd harmonic transverse voltage generated from these current-induced effective SOT fields componenets ($H_{DL}^{X,Y,Z}$, $H_{FL}^{X,Y,Z}$) and torques ($\tau_{DL}^{X,Y,Z}$, $\tau_{FL}^{X,Y,Z}$) in PMA ferromagnets is expressed as[28,29],

$$V_{xy}^{2\omega} = V_{DL}^Y \cos \Phi_B + V_{DL}^X \sin \Phi_B + V_{DL}^Z \cos 2\Phi_B + V_{FL}^Y \cos \Phi_B \cos 2\Phi_B$$
$$+ V_{FL}^X \sin \Phi_B \cos 2\Phi_B + V_{FL}^Z \quad (1)$$

Here, damping-like torque components generated by X, Y and Z spin polarization contribute to coefficients $V_{DL}^{X,Y,Z}$, and the field-like torque counterparts give rise to coefficients $V_{FL}^{X,Y,Z}$. The estimation of SOT fields ($H_{DL}^{X,Y,Z}$, $H_{FL}^{X,Y,Z}$) from coefficients ($V_{DL}^{X,Y,Z}$, $V_{FL}^{X,Y,Z}$) is detailed

in Supplementary Note 7 (Supplementary Eqs. S1–S7).

$$V_{xy}^{2\omega} = V_{DL} \cos \Phi_B + V_{FL} \cos \Phi_B \cos 2\Phi_B \quad (2)$$

The 2nd harmonic Hall signal as a function of Φ_B at constant fields ($H > H_K$) is plotted in Fig. 3b. The $V_{xy}^{2\omega}$ vs Φ_B curve is fitted with Eq. 2 to estimate SOT in materials containing only conventional in-plane spins[30,31]. However, $V_{xy}^{2\omega}$ vs Φ_B curve of TaIrTe$_4$/Fe$_3$GaTe$_2$ could not be well fitted with Eq. 2 (see Fig. 3b). For proper fitting, we need to include $V_{DL} \cos 2\Phi_B$ and $V_{DL} \sin \Phi_B$ terms as in Eq. 1, which consider additional torque components due to current-induced out-of-plane spin canting in TaIrTe$_4$. The coefficients $V_{xy\,\cos\Phi_B}^{2\omega}$, $V_{xy\,\sin\Phi_B}^{2\omega}$ and $V_{xy\,\cos 2\Phi_B}^{2\omega}$ are hyperbolic functions of the magnetic field (see Supplementary Note 7, Eqs S2–S4), implying linear function on $1/(H-H_K)$ or $1/H$. The values of these coefficients were extracted by fitting the experimental 2nd harmonic transverse voltage and plotted in Fig. 3c-e. From these slopes, $H_{DL}^{X,Y,Z}$ are estimated (using $R_{AHE} = 1\,\Omega$ and $R_{PHE} = 0.0113\,\Omega$; see Supplementary Note 6) and plotted as a function of current densities $J_{a.c.}$ in Fig. 3g. The slope of $H_{DL}^{X,Y,Z}$ vs $J_{a.c.}$ are found out to be $H_{DL}^X/J_{a.c.} \sim (3.09 \pm 0.37) \times 10^{-12}$ TA^{-1}m^2, $H_{DL}^Y/J_{a.c.} \sim (2.43 \pm 0.15) \times 10^{-12}$ TA^{-1}m^2 and $H_{DL}^Z/J_{a.c.} \sim (6.78 \pm 0.44) \times 10^{-12}$ TA^{-1}m^2. This analysis indicates that current-induced effective SOT fields or torques in TaIrTe$_4$/Fe$_3$GaTe$_2$ heterostructure originated from the out-of-plane spin polarization (σ^Z), and it is larger than its in-plane counterparts (σ^{XY}).

Tunable spin-orbit torque with temperature due to Fermi level tuning of TaIrTe$_4$

The polarity and magnitude of spin accumulation generated by TaIrTe$_4$ are influenced by the chemical potential[9], resulting in temperature dependence changes in the tilt angle (as shown in Fig. 1f). A similar trend is expected in the current-induced effective SOT fields or torques. Hence, to observe the temperature dependence of SOT efficiency from the 2nd harmonic Hall signal of TaIrTe$_4$/Fe$_3$GaTe$_2$, angle sweep second harmonic Hall (SHH) measurements are conducted at different temperatures. Figure 3f illustrates the $V_{xy}^{2\omega}$ vs Φ_B curve at 10 T across different temperatures. Damping-like SOT effective fields ($H_{DL}^{X,Y,Z}$) are estimated using Eq. 1. $H_{DL}^Z/J_{a.c.}$ is highly tunable with temperature (Fig. 3h), it decreased from 2 K to 100 K, reached a minimum between 100–200 K, and increased from 200 K to 325 K. This behavior aligns with the temperature dependence of current-induced spin accumulation (Fig. 1f), showing large out-of-plane spin polarization at 2 K and room temperature with a minimum near 100 K. Hence, the out-of-plane damping-like torque is observed to be tunable by the chemical potential of TaIrTe$_4$.

Field-dependent harmonic Hall measurements

To further validate and estimate SOT components, we measured the 1st and 2nd harmonic transverse Hall resistance R_{xy} signal as a function of magnetic field applied parallel to the sample surface ($H \perp c$) and perpendicular to the applied current direction. In the 1st harmonic R_{xy}^ω vs H, a hysteresis loop with a magnetic anisotropic field H_K of ~ 1.5 T is observed (Fig. 4a). The 2nd harmonics transverse Hall resistance signal $R_{xy}^{2\omega}$ varied with the external magnetic field applied parallel to the sample surface. The measurements are conducted with the field oriented either perpendicular (H_y, $\Phi_B = 90°$ or $270°$) or parallel (H_x, $\Phi_B = 0°$ or $180°$) to the direction of current (or a-axis of TaIrTe$_4$). These results are displayed in Fig. 4b, c. The resistance exhibited a hyperbolic dependence on the field for $|H| > H_k$, however became discontinuous for $|H| < H_K$.

Figure 4d, e shows 2nd harmonics transverse resistance ($R_{xy}^{2\omega}$) versus H_y and H_x for different applied sinusoidal current densities ($J_{a.c.}$). The hyperbolic curvature of these plots sharpens with increasing current
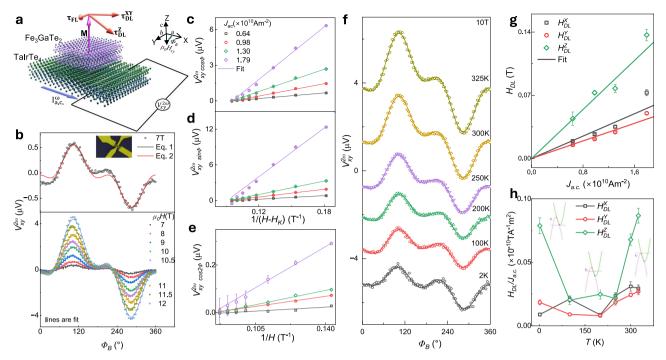
Fig. 3 | Angle-dependent harmonic Hall measurements in TaIrTe$_4$/Fe$_3$GaTe$_2$ heterostructure. a Schematic of the TaIrTe$_4$/Fe$_3$GaTe$_2$ heterostructure, illustrating the effects of damping-like torques (τ_{DL}^{XY} and τ_{DL}^Z) and field-like torques (τ_{FL}) on Fe$_3$GaTe$_2$ magnetization when the current is applied along the a-axis of TaIrTe$_4$ layer[19]. The 2nd harmonics Hall voltage ($V_{xy}^{2\omega}$) measurement scheme is shown with an external in-plane magnetic field at angle Φ_B relative to the a.c. current direction I_{ac}. **b** $V_{xy}^{2\omega}$ vs Φ_B of Dev1 at magnetic field 7 T and temperature 300 K. The solid lines are fitted with Eqs. 1 and 2. The second panel shows $V_{xy}^{2\omega}$ vs Φ_B for varied magnetic fields (7-12 T). **c–e** Coefficient $V_{xy\cos\Phi_B}^{2\omega}$ (cos Φ_B dependent in $V_{xy}^{2\omega}$), $V_{xy\sin\Phi_B}^{2\omega}$ (sin Φ_B dependent in $V_{xy}^{2\omega}$) and $V_{xy\cos2\Phi_B}^{2\omega}$ (cos 2ϕ_B dependent in V$_{xy}^{2\omega}$) as a function of 1/(H-

H$_k$) and 1/H under different current densities J$_{a.c.}$. The error bar in **c**, **d** and **e** are obtained from fitting of experimental data in (**b**) using Eq. 1. **f** Angle sweep of $V_{xy}^{2\omega}$ at different temperatures (2–325 K) at a constant magnetic field of 10 T. Solid lines are fit to experimental data using Eq. 1. **g** Damping-like field components (H_{DL}^X, H_{DL}^Y, H_{DL}^Z) as a function of current density, with linear fits estimating $H_{DL}/J_{a.c.}$, whereas error are obtained from the linear fit of **c**, **d** and **e** data. **h** Temperature dependence of $H_{DL}/J_{a.c.}$ for TaIrTe$_4$/Fe$_3$GaTe$_2$ device. Insets show the energy dispersion curve of type-II Weyl semimetal and tuning of Fermi level energy (E_F) with temperature. The error bars in (**h**) are obtained by fitting experimental data in (**f**) using Eq. 1.

density. For $R_{xy}^{2\omega}$ vs H_y data at $\Phi_B = 90°$ and $270°$, Eq. (1) reveals that only x and z components of the SOT fields contribute to the 2nd harmonics signal (see Supplementary Eq. S8). Therefore, from the analysis of $R_{xy}^{2\omega}$ vs H_y data at $\Phi_B = 90°$, we have calculated H_{DL}^X, H_{DL}^Z, H_{FL}^X and H_{FL}^Z. Similarly, for $R_{xy}^{2\omega}$ vs H_x data ($\Phi_B = 0°$) and using the extracted H_{DL}^Z and H_{FL}^Z values, we have estimated H_{DL}^Y and H_{FL}^Y (see Supplementary Eq. S9 and also see Supplementary Note 6 and 8). The extracted values of $H_{DL}^{X,Y,Z}$ with different current densities $J_{a.c.}$ are plotted in Fig. 4f. The slopes of H_{DL} vs $J_{a.c.}$ are found to be: $H_{DL}^X/J_{a.c.} \sim (0.348 \pm 0.081) \times 10^{-12}$ T A^{-1}m^2, $H_{DL}^Y/J_{a.c.} \sim (0.061 \pm 0.002) \times 10^{-12}$TA^{-1}m^2 and $H_{DL}^Z/J_{a.c.} \sim (3.50 \pm 0.27) \times 10^{-12}$TA^{-1}m^2. These findings also confirm that effective damping like the field corresponding to Z spin polarization is significantly larger than that from XY polarized spins.

It should be noted that TaIrTe$_4$ alone also exhibits a 2nd harmonic voltage signal as function of Φ_B, arising from broken mirror symmetry and finite Berry curvature dipole. This signal follows a cos Φ_B or sin Φ_B dependence (Fig. 1e). So, the H_{DL}^X and H_{DL}^Y values from the fitting of $V_{xy}^{2\omega}$ vs Φ_B data can be overestimated (Eq. 1). However, the estimation of Z-component damping-like field H_{FL}^Z using coefficient $V_{xy\cos2\Phi_B}^{2\omega}$ (Eq. 1), central to the conclusion of second harmonic measurements, remains consistent. Furthermore, only TaIrTe$_4$ also has a unique field dependence of 2nd harmonics signal as shown in Supplementary Fig. S6d, which is quite different from SOT-induced $R_{xy}^{2\omega}$ vs H curve (see Fig. 4b–e). At large magnetic field, the $R_{xy}^{2\omega}$ vs H curve from TaIrTe$_4$ appears to be linear function of magnetic field; hence, to account for the 2nd harmonics field contribution of TaIrTe$_4$ and thermal effects[31,32], a linear polynomial term is included while fitting the field-dependent curves (also see Supplementary Note 8). Also, the field-like torque for

Dev 1 and 2 and Nerst effect voltages for Dev1 are shown in Supplementary Fig. S7 and Supplementary Note 7.

Field-free deterministic spin-orbit torque switching in TaIrTe$_4$/Fe$_3$GaTe$_2$ heterostructure

SOT magnetization switching experiments are crucial for investigating magnetization switching characteristics, such as determining the critical switching current density, assessing the need for an external field to aid in switching, and identifying whether the process is deterministic or non-deterministic. A series of pulse currents (I_{pulse}) applied along the a-axis in the TaIrTe$_4$/Fe$_3$GaTe$_2$ heterostructure can induce an unconventional spin current along the z-axis, with spin polarization σ^Z oriented along the z-axis in TaIrTe$_4$[9]. This spin current generates an unconventional SOT on Fe$_3$GaTe$_2$, consisting of both field-like (τ_{FL}) and damping-like (τ_{DL}) torques, facilitating the switching of the magnetization direction **M**. The field-like torque $\tau_{FL} \sim \sigma \times m$ induces the precession of **M** around the exchange field generated by spin polarization, while the damping-like torque $\tau_{DL} \sim m \times (\sigma \times m)$ aligns **M** with the spin polarization σ, predominantly driving the magnetization switching (Fig. 5a)[33]. Figure 5b shows the AHE at 300 K of Dev3 used for switching experiments. Figure 5c presents SOT-induced magnetization switching, measured by applying a pulsed write current (I_p) along the a-axis with a pulse duration of 50 ms. This is followed by a small D.C. read current (I_r-500 µA) to determine the magnetization state via the Hall resistance R$_{xy}$=V$_{xy}$/I$_r$. Due to a large unconventional SOT, fully deterministic field-free magnetization switching could be observed at room temperature with I$_p$ = ±3.5 mA. Since the signal R$_{xy}$ is proportional to the out-of-plane magnetization M$_z$, the SOT R$_{xy}$ signal
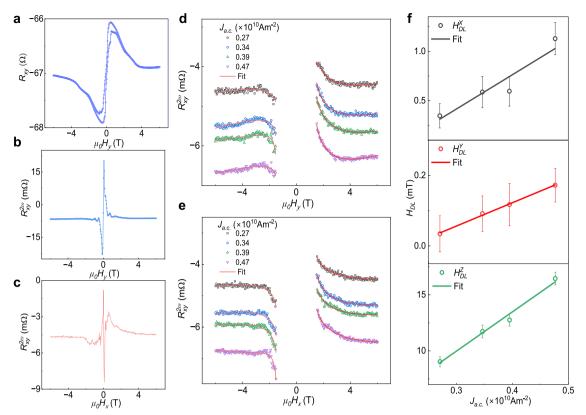
Fig. 4 | Field-dependent harmonic Hall measurements in TaIrTe$_4$/Fe$_3$GaTe$_2$ heterostructure. a 1st harmonic transverse resistance ($R_{xy}^{1\omega}$) as a function of magnetic field swept parallel to the sample surface ($H\perp c$) and perpendicular to current direction, measured at 300 K on Dev 2. **b, c** 2nd harmonic transverse resistance $R_{xy}^{2\omega}$ varied as a function of the external magnetic field applied along parallel to the sample surface, with H_y representing $H\perp c$ and perpendicular to the current ($H\perp J_{a.c.}$), and H_x representing $H\perp c$ and parallel to the current ($H\|J_{a.c.}$).

d, e Dependence of the 2nd harmonic transverse resistance ($R_{xy}^{2\omega}$) on the in-plane magnetic field (H_y and H_x) for different magnitudes of constant write current density ($J_{a.c.}$). The data is fitted using equations simplified from Supplementary Eq S1–S7 (also see Supplementary Eq. S8–S9 and Supplementary Note 8). **f** Extracted effective damping-like field components ($H_{DL}^{X,Y,Z}$) corresponding to spin polarization (σ^X, σ^Y, σ^Z) as a function of $J_{a.c.}$ along with corresponding error bars are obtained from fits to the 2nd harmonic signal.

indicates a current-induced magnetization change between +M_z and −M_z. Notably, deterministic SOT switching of TaIrTe$_4$/Fe$_3$GaTe$_2$ heterostructure is observed at $H_x = 0$ T, which indicates the creation of σ^Z spin polarization in TaIrTe$_4$ leading to an out-of-plane SOT component. The magnitude of the switching signal is comparable to the AHE signal magnitude with field sweep, showing a full magnetization switching[34–37].

We further investigated the impact of deterministic SOT switching on the external in-plane magnetic field parallel to the current direction (Fig. 5d). The external in-plane magnetic field (H_x) can break the symmetry of deterministic SOT switching. As the strength of H_x increases, the switching mechanism transitions from being predominantly driven by the out-of-plane spin torque component (τ_{DL}^z) to being influenced by the in-plane components ($\tau_{DL}^{x,y}$). We observed that a small positive H_x has minimal effect on the SOT switching signal, however, increasing H_x beyond 100 mT results in a noticeable reduction of the signal magnitude. Despite this reduction, the switching efficiency was maintained at 50%, demonstrating some robustness against the external magnetic field. In contrast, when H_x is applied in the negative direction, the switching efficiency drops significantly to about 50% even at −10 mT, and it nearly diminishes to -10% at -300 mT. Interestingly, the switching polarity remains unchanged up to 100 mT, indicating the effectiveness of the out-of-plane spin polarization of TaIrTe$_4$ in counteracting the external magnetic field[9,14]. In conventional SOT, where magnetization switching is driven purely by in-plane spin current, the switching polarity typically reverses abruptly with H_x[23,32]. However, this was not observed in our experiments, highlighting the larger contribution of τ_{DL}^z from TaIrTe$_4$ in the magnetization dynamics

of Fe$_3$GaTe$_2$. In device 4 (data provided in Supplementary Fig. S3), we observed that the switching polarity remained unchanged even up to 200 mT when pulse current of ±4 mA was applied along the a-axis of TaIrTe$_4$. However, it abruptly reversed when both the current and magnetic field of similar magnitude were applied along the b-axis of TaIrTe$_4$.

Furthermore, to examine the presence of τ_{DL}^z and calculate unconventional SOT driven switching efficiency, we have performed AHE loop shift measurement with bias current (see Supplementary Fig. S4)[38,39]. The out-of-plane antidamping torque can shift the AHE hysteresis loop when a positive and negative dc bias current beyond a threshold value equivalent to switching current density is applied along the a-axis of TaIrTe$_4$. Such AHE loop shift (H_{shift}) is observed for compensating τ_{DL}^z driven intrinsic damping in Fe$_3$GaTe$_2$[9,14,38]. The SOT efficiency (ε_{SOT}) due to unconventional τ_{DL}^z torque is defined by equation[39–41]

$$\varepsilon_{SOT} = \frac{2eM_s\eta t_{FM}}{\hbar}\frac{H_{shift}}{J_{switch}} \tag{3}$$

In our device, the ε_{SOT} is 1.76, with the H_{shift} and J_{switch} calculated to be 2 mT and 1.81×10^{10} Am^{-2}, respectively and M_s taken as 0.97×10^5 Am^{-1} (see Supplementary Note 5). The switching efficiency parameter (η), defined as the ratio of switching current-driven and magnetic field-driven AHE, is observed to be 1 (Fig. 5c). Using the device parameters ($\varepsilon_{SOT} = 1.76$ and charge conductivity of TaIrTe$_4$ $\sigma_c = 9.4 \times 10^5$ S/m), we estimate the spin Hall conductivity in TaIrTe$_4$/Fe$_3$GaTe$_2$ heterostructure to be $\sigma_{SH} = \hbar/2e(\varepsilon_{SOT}.\sigma_c) = 1.65\times10^6$ $\hbar/2e$ (Ωm)$^{-1}$. By
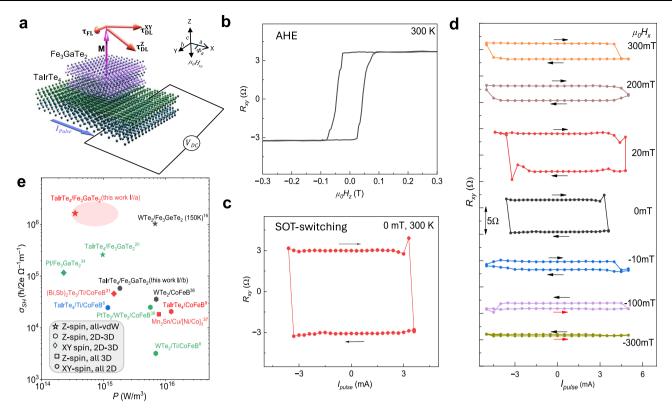
Fig. 5 | Energy-efficient, field-free deterministic magnetization switching by spin-orbit torque in the TaIrTe$_4$/Fe$_3$GaTe$_2$ heterostructure at room temperature. a Diagrammatic representation of TaIrTe$_4$/Fe$_3$GaTe$_2$ heterostructure. This configuration leads to a significant out-of-plane antidamping torque (τ_{AD}^{OOP}), which is symmetric with respect to the current direction, facilitating field-free deterministic switching of the Fe$_3$GaTe$_2$ magnetization[19]. **b** AHE of the TaIrTe$_4$/Fe$_3$GaTe$_2$ heterostructure device 3 with magnetic field sweep at 300 K. **c** Field-free full deterministic switching achieved at 3.5 mA pulse current and 500 µA current is used as reading current to measure magnetization states keeping external field zero at 300 K temperature. The current is applied along the symmetry axis (a-axis) of TaIrTe$_4$. **d** Current-driven magnetization switching of TaIrTe$_4$/Fe$_3$GaTe$_2$ under different bias fields parallel to the sample surface and current (H_x). The forward and backward current sweeps are distinguished by arrows. The data is vertically shifted to avoid overlap. **e** The benchmark of SOT spin Hall conductivity vs. power consumption with state-of-the-art results[8,9,16,31,34–37]. Ellipse represents error and device to device variation in the calculated parameters.

employing both SOT-induced magnetic switching and 2nd harmonic Hall measurements, we have established that the magnetization of Fe$_3$GaTe$_2$ in heterostructure with TaIrTe$_4$ can be effectively manipulated with a switching current density of $J_{switch} \sim 1.81 \times 10^{10}$ A/m^2 and power density P ($= J_{switch}^2/\sigma_c$) of 0.348×10^{15} $\frac{W}{m^3}$ at room temperature. The benchmarked of the spin Hall conductivity σ_{SH} and power density P of TaIrTe$_4$/Fe$_3$GaTe$_2$ devices along with literature available on state-of-the-art SOT devices[8,9,14–16,31,32,37,42] are shown in Fig. 5e and Supplementary Table 1.

Calculation of unconventional spin Hall effect in TaIrTe$_4$

Our experimental observations strongly suggest the presence of unconventional spin Hall effect in TaIrTe$_4$, which originates from the in-plane charge current and results in an out-of-plane spin-polarized spin current across the interface, corresponding the σ_{ZX}^Z component of the spin Hall conductivity (SHC) tensor ($I_Z^{S_Z} = \sigma_{ZX}^Z I_X^C$ where I^S and I^C are spin and charge currents, respectively). While similar effects were also found in another low-symmetry Weyl semimetal (T$_D$-WTe$_2$)[6,7,15,16,18], the symmetry constraints theoretically prohibit this configuration, and the experimental results have not been explained. Like WTe$_2$, TaIrTe$_4$ has low crystal symmetry described by space group (SG) 31 (Pmn2$_1$), consisting of a mirror plane perpendicular to the a axis (See Fig. 6a), as well as glide reflection and two-fold screw rotation, which prevents an unconventional SHC component[43].
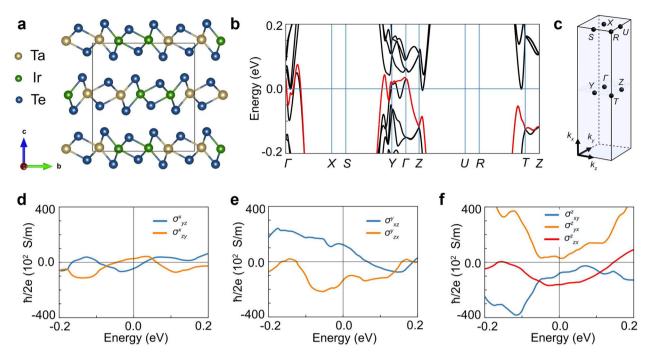
To unveil the origin of the unconventional SHE, we have performed first-principles calculations of TaIrTe$_4$ (see Methods for computational details). As shown in Fig. 6, our results reveal a large spin splitting of bands near the Fermi level due to SOC, and the presence of

seven spin Hall conductivity components: six conventional (σ_{jk}^i with $i \neq j \neq k$) and one unconventional component σ_{ZX}^Z, with the latter showing a magnitude comparable to the conventional components. The unconventional SHE at the Fermi level reaches $\sigma_{SH} = 1.56 \times 10^4$ $\hbar$/2e (Ωm)$^{-1}$, in agreement with experimental values reported for TaIrTe$_4$ (1.47–5.44)x10^4 $\hbar$/2e (Ωm)$^{-1}$ [8,9,18], which vary depending on experimental conditions and sample characteristics. Although previous studies attributed its presence to the topological properties of the surface[8], our calculations show that a large unconventional SHE occurs even in the bulk.

We analyzed the crystal symmetry in more detail by directly applying symmetry operations, revealing that the relaxed structures exhibit a slight deviation from SG 31. This small structural distortion reduces the symmetry to either SG 6 (Pm) or SG 1 (P1), depending on the specified numerical precision (see Supplementary Note 9 for details). In both cases, the two-fold screw symmetry which normally prohibits unconventional SHE is absent, thus allowing for out-of-plane spin polarization of spin current. Structural distortion could further increase near the surface, potentially enhancing the generated spin accumulation. Therefore, from a symmetry perspective, the unconventional SHE component is justified, while its magnitude arises from the electronic properties, as discussed in Supplementary Materials.

Discussion

Our experiments indicate even larger spin Hall conductivity (SHC) values than previously reported and reveal an additional component, σ_{ZY}^Z, induced by charge current along the mirror plane. This component was absent in the previous studies and does not emerge in bulk

Fig. 6 | Electronic structure and spin Hall conductivity calculations of TaIrTe$_4$. **a** Orthorhombic crystal unit cell of TaIrTe$_4$. **b** Electronic structure of TaIrTe$_4$ calculated via density functional theory along the high-symmetry lines in the Brillouin zone shown in **c**. **d**–**f** Calculated intrinsic spin Hall conductivity, representing configurations of spin current with spin polarization along a-, b-, and c-axis, respectively. The magnitude of the unconventional spin Hall conductivity σ_{zx}^z at the Fermi level is determined mostly by the band marked as red in **b**.

calculation, suggesting a possible role of interfacial effects. The overall enhancement of SHC could arise from the spin and orbital effects at the TaIrTe$_4$/Fe$_3$GaTe$_2$ interfaces, and also from the individual constituents[12,42,44–52]. This highlights the unique behaviors of the vdW heterostructure and suggests unfamiliar avenues for exploring SOT in low-symmetry materials.

In summary, we demonstrated the potential of TaIrTe$_4$/Fe$_3$GaTe$_2$ vdW heterostructures for generating a large and tunable nonlinear 2nd harmonic Hall effect, and energy-efficient deterministic field-free magnetization switching at room temperature. By leveraging the unique properties of the topological Weyl semimetal TaIrTe$_4$ and the magnetic Fe$_3$GaTe$_2$ with strong PMA, our findings reveal a large nonlinear Hall effect, substantial unconventional out-of-plane damping-like torque and a remarkably low switching current density, outperforming conventional systems. To unveil the origin of unconventional charge-spin conversion phenomena in TaIrTe$_4$, detailed first-principles calculations were performed considering crystal symmetry and its impact on the energy-dependent electronic structure and spin Hall conductivity. Finally, we measured a substantial and tunable damping-like torque and observed deterministic field-free magnetization switching at a very low current density offering a promising route to energy-efficient and external field-free spintronic technologies.

Note: After preparation of this manuscript, we came across reports on magnetization switching in TaIrTe$_4$/Fe$_3$GaTe$_2$ system[34,53]. However, spin dynamics experiments to understand the spin-orbit torque phenomena in vdW heterostructures are so far lacking. In our manuscript, in addition to energy-efficient magnetization switching, we report a detailed understanding of unconventional and tunable SOT magnetization dynamics using 2nd harmonic measurements in all-vdW heterostructures.

We have observed a larger out-of-plane damping-like torque compared to the in-plane components in heterostructures of TaIrTe$_4$/Fe$_3$GaTe$_2$. This conclusion is drawn from measurements on various devices (Dev1-Dev5) across different experimental setups, thereby reinforcing the reproducibility and robustness of this finding. However, the ratio of magnitude of H_{DL}^Z/H_{DL}^{XY} varies among devices, indicating a more profound role of spin Hall conductivity that can arise from the spin and orbital effects at the TaIrTe$_4$/Fe$_3$GaTe$_2$ interfaces. This variation may be influenced by the relative twist angle between the incommensurate heterostructures of TaIrTe$_4$ and Fe$_3$GaTe$_2$, which requires further investigation[54].

Methods

Single crystal growth

TaIrTe$_4$ single crystals were synthesized by evaporating tellurium from a Ta-Ir-Te melt, with the crystal growth conducted at 850 °C and Te condensation at 720 °C[55]. Fe$_3$GaTe$_2$ single crystals were grown via a self-flux method using Fe, Ga, and Te with 99.99% purity in the molar ratio of 1:1:2 in an evacuated and sealed quartz tube. The solid reactions took place for 24 h at 1273 K, followed by cooling to 1153 K within 1 h and slowly cooling down to 1053 K within 100 h[10].

Device fabrication

The van der Waals heterostructure samples were prepared by mechanically exfoliating nanolayers of TaIrTe$_4$ and Fe$_3$GaTe$_2$ crystals on top of each other on a SiO$_2$/Si wafer using the Scotch tape method inside a glove box. The top sample surface was immediately capped with a 2 nm Al$_2$O$_3$ layer to protect from degradation with time. For the Devs1-3 nearly rectangular-shaped flakes were selected and the TaIrTe$_4$/Fe$_3$GaTe$_2$ heterostructures were patterned to Hall-bar geometry using electron-beam lithography (EBL) and Ti (15 nm)/Au (250 nm) contacts were prepared by EBL and electron beam evaporation. For Dev4 and Dev5, flakes are in arbitrary shapes, therefore, dry physical etching by Ar ion milling was used to fabricate well-defined Hall-bar devices.

Spin-orbit torque 2nd harmonic measurements

Spin-orbit torque was characterized using an in-plane 2$^{2\omega}$ harmonic Hall lock-in measurement technique. The $R_{xy}^{1\omega}$ and $R_{xy}^{2\omega}$ for an a.c.

current I^ω of 213.3 Hz were simultaneously measured while rotating the sample in the plane (azimuthal angle φ_B) under an external field $\mu_O H_{ext}$. The harmonic measurements were conducted using a Lock-in SR830 to detect the in-phase 1st and out-of-phase 2nd harmonic voltages. The 2nd harmonic measurements in the high magnetic field range were performed with a Quantum Design cryogen-free PPMS DynaCool system, interfaced with the SR830 to record the 1st and 2nd harmonic voltages. The 1st harmonic signal is detected by putting the voltmeter in phase with the oscillator, whereas the 2nd harmonic signal is out of phase with the source signal.

Spin-orbit torque switching measurements were conducted in a vacuum cryostat with a magnetic field strength of up to 0.7 T. Electronic measurements were carried out using a Keithley 6221 current source and a Keithley 2182 A nanovoltmeter. To monitor the longitudinal and transverse Hall resistances, Keithley 2182 A nanovoltmeters were employed. For SOT-induced magnetization switching, the Keithley 2182 A nanovoltmeters were used to observe the Hall resistances responses, while a Keithley 6221 A.C. source applied a pulse current of 50 millisecond (ms) through the device, followed by a D.C. read current of magnitude 500 μA.

Density functional calculations

Density functional theory calculations for bulk TaIrTe₄ were performed using the Quantum Expresso package[56,57] by employing the Perdew, Burke, and Ernzerhof (PBE) generalized gradient approximation (GGA) for exchange-correlation functional[58]. We used fully relativistic pseudopotentials and expanded the electron wave functions in a plane-wave basis with the energy cutoff of 80 Ry. We adopted an orthorhombic unit cell with the experimental lattice constants $a = 3.77$ Å, $b = 12.42$ Å, and $c = 13.18$ Å[59]. The atomic positions were relaxed with the force and energy convergence thresholds set to 10^{-3} Ry/Bohr and 10^{-4} Ry, respectively. The Brillouin Zone (BZ) was sampled following the Monkhorst-Pack scheme with the k-grids of $20 \times 8 \times 8$ and adopting a Gaussian smearing of 10^{-3} Ry. For the post-processing analysis, we used the python package PAOFLOW, which projects the ab initio wavefunctions onto pseudo-atomic orbital (PAO) basis to construct tight-binding Hamiltonians[60,61], further interpolated to a denser grid of $80 \times 40 \times 40$. The charge-to-spin conversion response tensors were calculated using the approaches implemented in PAOFLOW and described in the previous works[62–64].

Data availability

The data that support the findings of this study are available from the corresponding authors on a reasonable request.

References

1. Manchon, A. et al. Current-induced spin-orbit torques in ferromagnetic and antiferromagnetic systems. *Rev. Mod. Phys.* **91**, 035004 (2019).
2. Shao, Q. et al. Roadmap of spin–orbit torques. *IEEE Trans. Magn.* **57**, 1–39 (2021).
3. Han, W., Otani, Y. & Maekawa, S. Quantum materials for spin and charge conversion. *npj Quant. Mater.* **3**, 27 (2018).
4. Liu, L. et al. Spin-torque switching with the giant spin Hall effect of Tantalum. *Science* **336**, 555–558 (2012).
5. Gong, C. et al. Discovery of intrinsic ferromagnetism in two-dimensional van der Waals crystals. *Nature* **546**, 265–269 (2017).
6. Zhao, B. et al. Unconventional charge–spin conversion in Weyl-Semimetal WTe₂. *Adv. Mater.* **32**, 2000818 (2020).
7. Zhao, B. et al. Observation of charge to spin conversion in Weyl semimetal WTe₂ at room temperature. *Phys. Rev. Res.* **2**, 013286 (2020).
8. Zhang, Y. et al. Room temperature field-free switching of perpendicular magnetization through spin-orbit torque originating from low-symmetry type II Weyl semimetal. *Sci. Adv.* **9**, eadg9819 (2023).
9. Liu, Y. et al. Field-free switching of perpendicular magnetization at room temperature using out-of-plane spins from TaIrTe₄. *Nat. Electron* **6**, 732–738 (2023).
10. Zhang, G. et al. Above-room-temperature strong intrinsic ferromagnetism in 2D van der Waals Fe₃GaTe₂ with large perpendicular magnetic anisotropy. *Nat. Commun.* **13**, 5067 (2022).
11. Wang, X. et al. Current-driven magnetization switching in a van der Waals ferromagnet Fe₃GeTe₂. *Sci. Adv.* **5**, eaaw8904 (2019).
12. Zhang, K. et al. Gigantic current control of coercive field and magnetic memory based on nanometer-thin ferromagnetic van der Waals Fe₃GeTe₂. *Adv. Mater.* **33**, 2004110 (2021).
13. Zhao, B. et al. Coexisting non-trivial van der Waals magnetic orders enable field-free spin-orbit torque magnetization dynamics. *Adv. Mater.* **37**, 2502822 (2025).
14. Kao, I.-H. et al. Deterministic switching of a perpendicularly polarized magnet using unconventional spin–orbit torques in WTe₂. *Nat. Mater.* **21**, 1029–1034 (2022).
15. Kajale, S. N., Nguyen, T., Hung, N. T., Li, M. & Sarkar, D. Field-free deterministic switching of all–van der Waals spin-orbit torque system above room temperature. *Sci. Adv.* **10**, eadk8669 (2024).
16. Shin, I. et al. Spin–Orbit Torque switching in an all-Van der Waals heterostructure. *Adv. Mater.* **34**, 2101730 (2022).
17. Pan, Z.-C. et al. Room-temperature orbit-transfer torque enabling van der Waals magnetoresistive memories. *Sci. Bull.* **68**, 2743–2749 (2023).
18. Bainsla, L. et al. Large out-of-plane spin–orbit torque in topological Weyl semimetal TaIrTe₄. *Nat. Commun.* **15**, 4649 (2024).
19. Momma, K. & Izumi, F. VESTA 3 for three-dimensional visualization of crystal, volumetric and morphology data. *J. Appl. Crystallogr.* **44**, 1272–1276 (2011).
20. Koepernik, K. et al. TaIrTe₄: a ternary type-II Weyl semimetal. *Phys. Rev. B* **93**, 201101 (2016).
21. Kumar, D. et al. Room-temperature nonlinear Hall effect and wireless radiofrequency rectification in Weyl semimetal TaIrTe₄. *Nat. Nanotechnol.* **16**, 421–425 (2021).
22. He, P. et al. Bilinear magnetoelectric resistance as a probe of three-dimensional spin texture in topological surface states. *Nat. Phys.* **14**, 495–499 (2018).
23. Li, W. et al. Room-temperature van der Waals ferromagnet switching by spin-orbit torques. *Adv. Mater.* **35**, 2303688 (2023).
24. Herring, C. & Kittel, C. On the theory of spin waves in ferromagnetic media. *Phys. Rev.* **81**, 869–880 (1951).
25. Sato, K. et al. Weak itinerant ferromagnetism in Heusler-type Fe₂VAl₀.₉₅. *Phys. Rev. B* **82**, 104408 (2010).
26. Mishra, V. et al. Investigation of spin gapless semiconducting behaviour in quaternary CoFeMnSi Heusler alloy thin films on Si (1 0 0). *J. Magn. Magn. Mater.* **547**, 168837 (2022).
27. Miron, I. M. et al. Perpendicular switching of a single ferromagnetic layer induced by in-plane current injection. *Nature* **476**, 189–193 (2011).
28. Wu, H. et al. Room-temperature spin-orbit torque from topological surface states. *Phys. Rev. Lett.* **123**, 207205 (2019).
29. Bose, A. et al. Tilted spin current generated by the collinear antiferromagnet ruthenium dioxide. *Nat. Electron* **5**, 267–274 (2022).
30. Takeuchi, Y. et al. Spin-orbit torques in high-resistivity-W/CoFeB/MgO. *Appl. Phys. Lett.* **112**, 192408 (2018).
31. Kajale, S. N. et al. Current-induced switching of a van der Waals ferromagnet at room temperature. *Nat. Commun.* **15**, 1485 (2024).
32. Wang, H. et al. Room temperature energy-efficient spin-orbit torque switching in two-dimensional van der Waals Fe₃GeTe₂ induced by topological insulators. *Nat. Commun.* **14**, 5173 (2023).

33. Zhu, L. Switching of perpendicular magnetization by spin–orbit torque. *Adv. Mater.* **35**, 2300853 (2023).

34. Zhang, Y. et al. Robust field-free switching using large unconventional spin-orbit torque in an all-Van der Waals heterostructure. *Adv. Mater.* **36**, 2406464 (2024).

35. Wang, X. et al. Room temperature field-free switching of CoFeB/MgO heterostructure based on large-scale few-layer WTe_2. *Cell Rep. Phys. Sci.* **4**, 101468 (2023).

36. Hu, S. et al. Efficient perpendicular magnetization switching by a magnetic spin Hall effect in a noncollinear antiferromagnet. *Nat. Commun.* **13**, 4447 (2022).

37. Wang, F. et al. Field-free switching of perpendicular magnetization by two-dimensional $PtTe_2$/WTe_2 van der Waals heterostructures with high spin Hall conductivity. *Nat. Mater.* **23**, 768–774 (2024).

38. Yu, G. et al. Switching of perpendicular magnetization by spin–orbit torques in the absence of external magnetic fields. *Nat. Nanotech.* **9**, 548–554 (2014).

39. Pai, C.-F., Mann, M., Tan, A. J. & Beach, G. S. D. Determination of spin torque efficiencies in heterostructures with perpendicular magnetic anisotropy. *Phys. Rev. B* **93**, 144409 (2016).

40. Nguyen, M.-H. et al. Enhancement of the anti-damping spin torque efficacy of platinum by interface modification. *Appl. Phys. Lett.* **106**, 222402 (2015).

41. Pai, C.-F., Ou, Y., Vilela-Leão, L. H., Ralph, D. C. & Buhrman, R. A. Dependence of the efficiency of spin Hall torque on the transparency of Pt/ferromagnetic layer interfaces. *Phys. Rev. B* **92**, 064426 (2015).

42. Choi, G. S. et al. Highly efficient room-temperature spin-orbit-torque switching in a van der Waals heterostructure of topological insulator and ferromagnet. *Adv. Sci.* **11**, 2400893 (2024).

43. Roy, A., Guimarães, M. H. D. & Sławińska, J. Unconventional spin Hall effects in nonmagnetic solids. *Phys. Rev. Mater.* **6**, 045004 (2022).

44. Zhang, G. et al. Room-temperature highly-tunable coercivity and highly-efficient multi-states magnetization switching by small current in single 2D ferromagnet Fe_3GaTe_2. *ACS Mater. Lett.* **6**, 482–488 (2024).

45. Deng, Y. et al. Room-temperature highly efficient nonvolatile magnetization switching by current in van der Waals Fe_3GaTe_2 devices. *Nano Lett.* **24**, 9302–9310 (2024).

46. Zhang, K. et al. Highly efficient nonvolatile magnetization switching and multi-level states by current in single van der Waals topological ferromagnet Fe_3GeTe_2. *Adv. Funct. Mater.* **31**, 2105992 (2021).

47. Johansen, Ø, Risinggård, V., Sudbø, A., Linder, J. & Brataas, A. Current control of magnetism in two-dimensional Fe_3GeTe_2. *Phys. Rev. Lett.* **122**, 217203 (2019).

48. Cui, J., Zhang, K.-X. & Park, J.-G. All van der Waals three-terminal SOT-MRAM realized by topological ferromagnet Fe_3GeTe_2. *Adv. Electron. Mater.* **10**, 2400041 (2024).

49. Martin, F. et al. Strong bulk spin–orbit torques quantified in the van der Waals ferromagnet Fe_3GeTe_2. *Mater. Res. Lett.* **11**, 84–89 (2023).

50. Robertson, I. O. et al. Imaging current control of magnetization in Fe_3GeTe_2 with a widefield nitrogen-vacancy microscope. *2D Mater.* **10**, 015023 (2022).

51. Zhang, K.-X. et al. Broken inversion symmetry in van der Waals topological ferromagnetic metal iron germanium telluride. *Adv. Mater.* **36**, 2312824 (2024).

52. Canonico, L. M., García, J. H., Cummings, A. W. & Roche, S. Spin Polarization driven by itinerant orbital angular momentum in van der Waals heterostructures. Preprint at arXiv https://doi.org/10.48550/arXiv.2507.12587 (2025).

53. Li, D. et al. Room-temperature van der Waals magnetoresistive memories with data writing by orbital current in the Weyl semimetal $TaIrTe_4$. *Phys. Rev. B* **110**, 035423 (2024).

54. Carr, S. et al. Twistronics: manipulating the electronic properties of two-dimensional layered structures through their twist angle. *Phys. Rev. B* **95**, 075420 (2017).

55. Chareev, D. A. et al. Growth of transition-metal dichalcogenides by solvent evaporation technique. *Cryst. Growth Des.* **20**, 6930–6938 (2020).

56. Giannozzi, P. et al. QUANTUM ESPRESSO: a modular and open-source software project for quantum simulations of materials. *J. Phys. Condens. Matter* **21**, 395502 (2009).

57. Giannozzi, P. et al. Advanced capabilities for materials modelling with Quantum ESPRESSO. *J. Phys. Condens. Matter* **29**, 465901 (2017).

58. Perdew, J. P., Burke, K. & Ernzerhof, M. Generalized gradient approximation made simple. *Phys. Rev. Lett.* **77**, 3865–3868 (1996).

59. Mar, A., Jobic, S. & Ibers, J. A. Metal-metal vs tellurium-tellurium bonding in WTe_2 and its ternary variants $TaIrTe_4$ and $NbIrTe_4$. *J. Am. Chem. Soc.* **114**, 8963–8971 (1992).

60. Buongiorno Nardelli, M. et al. PAOFLOW: a utility to construct and operate on ab initio Hamiltonians from the projections of electronic wavefunctions on atomic orbital bases, including characterization of topological materials. *Comput. Mater. Sci.* **143**, 462–472 (2018).

61. Cerasoli, F. T. et al. Advanced modeling of materials with PAOFLOW 2.0: New features and software design. *Comput. Mater. Sci.* **200**, 110828 (2021).

62. Sławińska, J. et al. Giant spin Hall effect in two-dimensional monochalcogenides. *2D Mater.* **6**, 025012 (2019).

63. Roy, A. et al. Long-range current-induced spin accumulation in chiral crystals. *npj Comput Mater.* **8**, 243 (2022).

64. Tenzin, K. et al. Analogs of Rashba-Edelstein effect from density functional theory. *Phys. Rev. B* **107**, 165140 (2023).

Acknowledgements

Author contributions

L.P. and S.P.D. conceived the idea and designed the experiments. L.P. fabricated and characterized the devices with support from B.Z., R.N., L.S., H.B., and P.R. The $TaIrTe_4$ single crystals were grown by A.A. and M.A.H., while G.Z., H.W., and H.C. grew the Fe_3GaTe_2 single crystals. K.T., V.L., and J.S. performed, analyzed and described the density functional theory calculations. J.S. supervised theoretical calculations. L.P. and S.P.D. analyzed and interpreted the experimental data and wrote the manuscript, with comments from all the authors. S.P.D. coordinated and supervised the project.

Funding

Competing interests

The authors declare no competing interests.

Additional information

Supplementary information The online version contains supplementary material available at
https://doi.org/10.1038/s41467-025-64109-3.

Correspondence and requests for materials should be addressed to Lalit Pandey or Saroj P. Dash.

Peer review information *Nature Communications* thanks Deblina Sarkar who co-reviewed with Shivam Kajale and the other, anonymous, reviewer(s) for their contribution to the peer review of this work. A peer review file is available.

Reprints and permissions information is available at
http://www.nature.com/reprints

Publisher's note Springer Nature remains neutral with regard to jurisdictional claims in published maps and institutional affiliations.